

Detecting Broken Rotor Bars With Zero-Setting Protection

Carlos Pezzani, Pablo Donolo, and Guillermo Bossio
Universidad Nacional de Río Cuarto

Marcos Donolo, Armando Guzmán, and Stanley E. Zocholl
Schweitzer Engineering Laboratories, Inc.

© 2012 IEEE. Personal use of this material is permitted. Permission from IEEE must be obtained for all other uses, in any current or future media, including reprinting/republishing this material for advertising or promotional purposes, creating new collective works, for resale or redistribution to servers or lists, or reuse of any copyrighted component of this work in other works.

This paper was published in *IEEE Transactions on Industry Applications*, Volume 50, Issue 2, and can be accessed at: <http://dx.doi.org/10.1109/TIA.2013.2276116>.

This paper was previously presented at the 48th Annual Industrial & Commercial Power Systems Technical Conference and can be accessed at: <http://dx.doi.org/10.1109/ICPS.2012.6229616>.

For the complete history of this paper, refer to the next page.

Published in

IEEE Transactions on Industry Applications, Volume 50, Issue 2, March/April 2014

Previously presented at the

48th Annual Industrial & Commercial Power Systems Technical Conference, May 2012

Originally presented at the

38th Annual Western Protective Relay Conference, October 2011

Detecting Broken Rotor Bars With Zero-Setting Protection

Carlos Pezzani,
Pablo Donolo, and
Guillermo Bossio
Universidad Nacional
de Río Cuarto
Ruta Nac. 36 – Km. 601
Río Cuarto, Córdoba
X5804BYA
Argentina

Marcos Donolo
Senior Member, IEEE
Schweitzer Engineering
Laboratories, Inc.
2350 NE Hopkins Court
Pullman, WA 99163, USA
marcos_donolo@selinc.com

Armando Guzmán
Senior Member, IEEE
Schweitzer Engineering
Laboratories, Inc.
2350 NE Hopkins Court
Pullman, WA 99163, USA
armando_guzman@selinc.com

Stanley E. Zocholl
Life Fellow, IEEE
Schweitzer Engineering
Laboratories, Inc.
2350 NE Hopkins Court
Pullman, WA 99163, USA
stan_zocholl@selinc.com

Abstract—Broken rotor bars in induction motors can be dependably detected by analyzing the current signatures under sufficient motor load conditions. Detection becomes less dependable under light motor load conditions. There are also cases in which tolerable motor operating conditions generate current signatures similar to those of motors with broken rotor bars. These cases may present security concerns when the detection element is set to trip the motor and to send alarms.

In this paper, we:

- Show how broken rotor bars cause characteristic current signatures.
- Show how to detect broken rotor bars with a zero-setting protection element, which uses the current signature method.
- Use cases with different motor operating and fault conditions to analyze the performance of the zero-setting broken bar protection element.
- Identify cases when the current signature method is dependable and cases when security is a concern.
- Present solutions to address security concerns.

Index Terms—Induction motor protection, broken rotor bars, squirrel cage rotor, induction motor relaying, condition monitoring.

I. INTRODUCTION

Induction motors are an important part of many industrial processes. Identifying motor failures in the early stages is critical to improve process productivity and minimize motor damage. Technical personnel in charge of industrial sites require motor protection relays that are easy to commission and provide prompt alarming of motor failures. According to surveys by the Electric Power Research Institute (EPRI) (see Fig. 1) and IEEE, 5 percent of motor failures happen because of problems in the rotor cage [1] [2].

Early detection of a broken rotor bar minimizes motor damage and reduces repair costs. In some cases, the broken bar condition starts with a fracture at the junction between the rotor bar and the end ring as a result of thermal and mechanical stresses [3]. These stresses are more significant when starting motors with high-inertia loads. The bending of a

fractured bar due to changes in temperature causes the bar to break. When one bar breaks, the adjacent bars carry currents greater than their design values, causing more damage if the broken bar condition is not promptly detected. Interbar currents that appear because of the broken bar affect the evolution of the fault in the rotor, causing damage in the laminations of the rotor core [3].

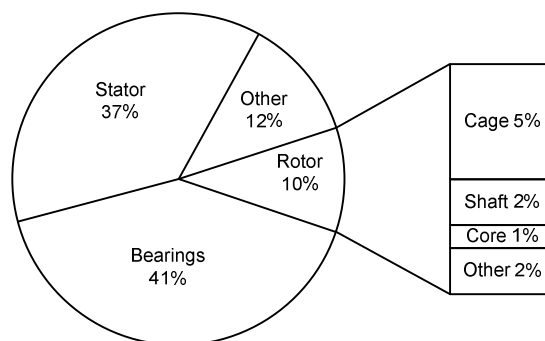


Fig. 1. EPRI survey results indicate that 5 percent of motor faults are because of rotor cage faults.

Motor current signature analysis (MCSA) is the most popular method to detect rotor cage faults [4] [5]. This method performs frequency spectrum analysis of the stator currents to determine the electromechanical conditions of the motor and the driven equipment. When one or more bars break, upper and lower sidebands appear at $(1 \pm 2s)f_o$, where s is the motor slip frequency and f_o is the system frequency [6]. The magnitudes of these sidebands increase with the number of broken bars.

In this paper, we describe a protection element that determines the number of broken bars using the relative magnitudes of the signals at the sideband frequencies ($\pm 2sf_o$) caused by the broken bars, with respect to the signal magnitude at the system frequency (f_o). This normalization allows the algorithm to identify rotor failures independent of motor characteristics.

Loads such as compressors, pumps, mills, and machines with gear boxes cause amplitude modulation in the stator currents with corresponding sideband frequencies at $f_o \pm f_r$,

$f_0 \pm 2f_r$, $f_0 \pm 3f_r$, and so on, where f_r is the output frequency associated with the speed of rotation of the driven load [7]. In some applications, sideband frequencies at $\pm f_r$, $\pm 2f_r$, and $\pm 3f_r$ may affect the magnitudes of the sidebands caused by broken bar conditions ($\pm 2sf_0$), making the proposed approach unsuitable for these applications. For this reason, the proposed solution also includes a Fourier transform function for analysis by a motor expert.

We describe a protective relay with the following features for motor monitoring and protection:

- A broken rotor bar detection element (BBDE) that uses MCSA for continuous monitoring and early detection of broken rotor bars.
- A history report that includes the date and time of the BBDE operations along with the maximum sideband magnitude and associated frequency. These data help correlate the BBDE operations to other events in the industrial plant.
- A Fourier transform function that calculates the frequency spectrum of the stator currents or voltages for motor diagnostics in cases when other sideband frequencies appear.

The paper also presents the results of the BBDE performance for actual motors, including a 5.5 kW motor, a 55 kW motor, and a 1.656 MW motor.

II. SIMULATIONS OF A MOTOR WITH BROKEN BARS

A. Induction Motor Model

We use the multiple-coupled circuit model described in [8] to analyze the harmonic content of the stator currents when a motor has broken bars. The rotor cage portion of the model for a healthy motor consists of n identical and equally spaced current loops formed by two rotor bars and two end ring segments (see Fig. 2). R_b and L_b represent the resistance and leakage inductance of each bar. R_e and L_e represent the resistance and leakage inductance of each end ring segment between adjacent bars. This model does not consider saturation, parasitic currents, and interbar currents but still shows the effect of the broken bars on the stator currents.

Fig. 3 shows the squirrel cage equivalent circuit for a motor with one broken bar, as described in [9] and [10]. This circuit eliminates the loop n and modifies the self-inductance and mutual inductance associated with the loop $n - 1$. We use a similar procedure to simulate two or three broken bars.

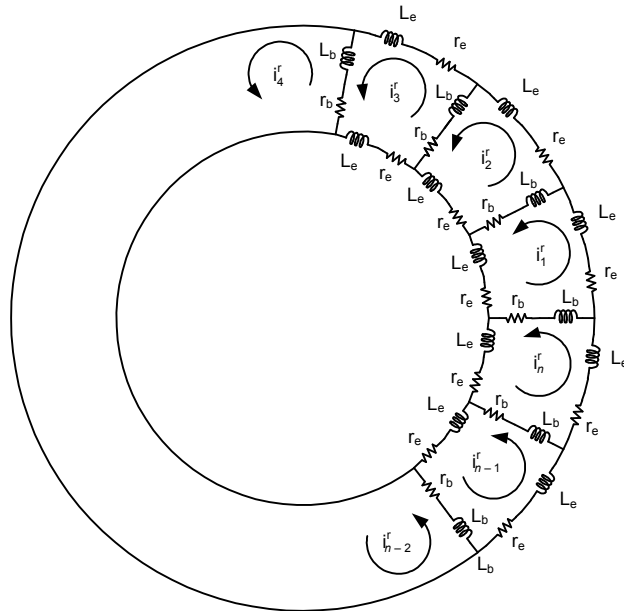


Fig. 2. Squirrel cage equivalent circuit for a healthy motor.

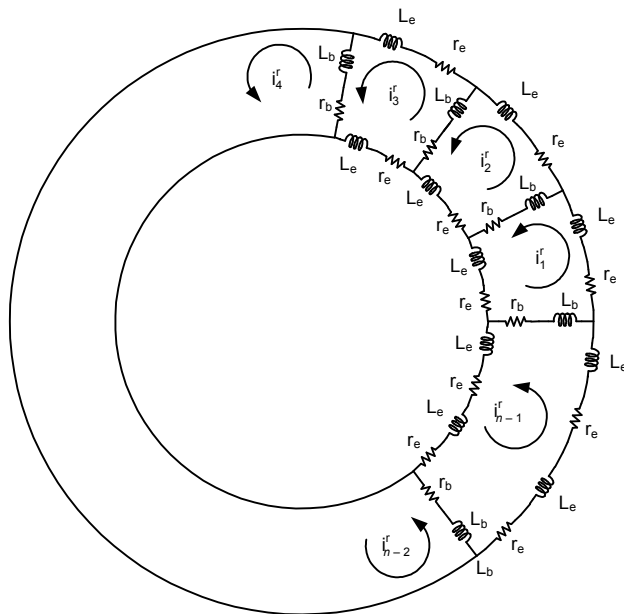


Fig. 3. Squirrel cage equivalent circuit for a motor with one broken bar.

B. Simulation Results

We modeled a motor with one, two, and three broken bars to analyze the harmonic content of the stator currents for these operating conditions. Appendix A includes the technical data and parameters of the induction motor that we used in our model.

1) Frequency Spectrum of the Phase Current of a Motor With Three Broken Bars

We applied balanced voltages to a motor model that simulates three broken bars. As seen in Fig. 4, the phase current exhibits an amplitude modulation because of the broken bar condition.

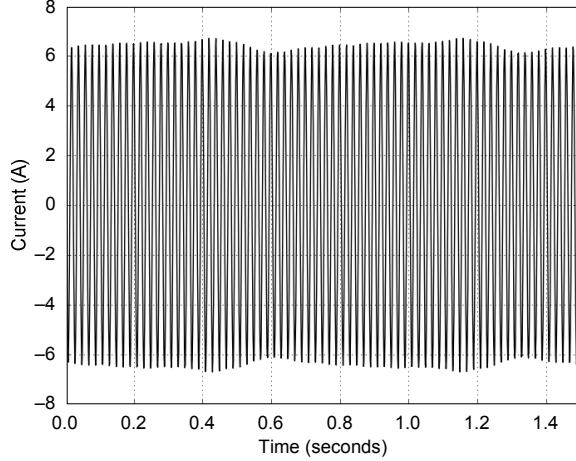


Fig. 4. Motor A-phase current for three broken bars.

Fig. 5 shows the frequency spectrum of the A-phase stator current when the motor has three broken bars. The magnitudes of the current components are normalized with respect to the magnitude of the fundamental current component. In this simulation, the motor operates at nominal load. As expected, the sidebands appear around the fundamental component ($f_0 = 50$ Hz) at frequencies $(1 \pm 2k)s)f_0$, where $k = 1, 2, 3$, and so on.

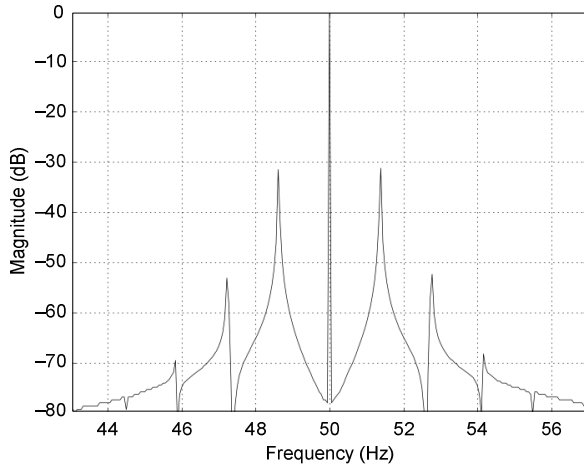


Fig. 5. Fundamental and sideband components for three broken bars.

2) Relative Current Magnitudes of a Motor With One, Two, and Three Broken Bars

Fig. 6 shows the relative magnitudes of the A-phase current components at the lower and upper sideband frequencies with respect to the magnitudes at fundamental frequency for one, two, and three broken bars. We observe that for these operating conditions, the relative magnitudes are a good indicator to determine the number of broken bars.

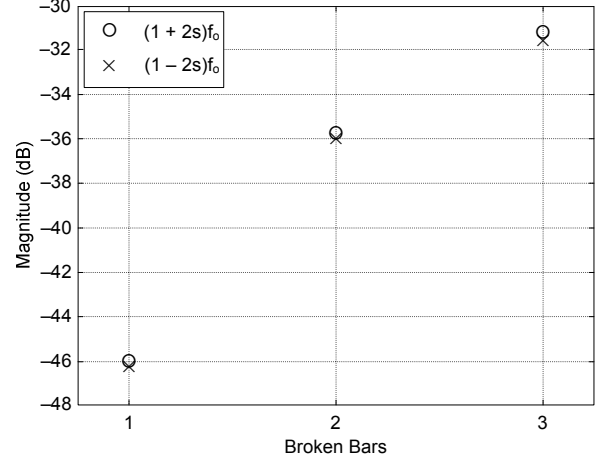


Fig. 6. Relative magnitudes of the phase current components at the sidebands with respect to the magnitude of the fundamental current component for one, two, and three broken bars.

III. A METHOD FOR DETECTING BROKEN BARS

A. Broken Bar Detection Element With Zero Settings

The BBDE runs periodically regardless of the status of the motor. Every time the BBDE runs, the BBDE goes through three phases: initialization, data collection, and data processing, as Fig. 7 illustrates.

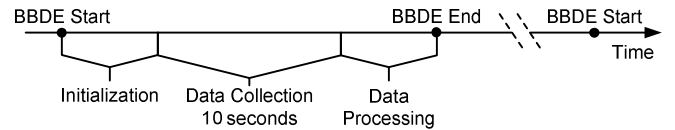


Fig. 7. Broken rotor bar detection process.

B. Initialization Phase

During the initialization phase, the relay records the initial magnitude of the alpha current, I_{α} , (1) and the initial system frequency. The relay uses these values as a reference to verify that the motor is operating under steady-state conditions during the data collection phase.

$$I_{\alpha} = \frac{2I_a - (I_b + I_c)}{3} \quad (1)$$

C. Data Collection Phase

The data collection phase starts after the element initialization phase ends. In this phase, the relay collects alpha current data, I_α , while monitoring that the motor operates under steady-state conditions. Fig. 8 shows the data collection logic.

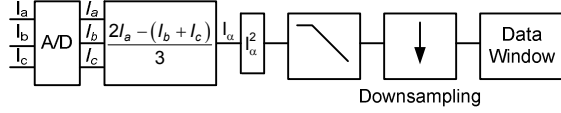


Fig. 8. Alpha current data collection.

The BBDE samples the motor currents and computes I_α as shown in Fig. 8. I_α is then squared to move the broken bar frequency components from $(1 + 2s)f_0$ Hz and $(1 - 2s)f_0$ Hz to $2s$ Hz, where s is the motor slip and f_0 is the power system frequency. In addition to decoupling the frequency of interest from the power system frequency, squaring the signal moves both sidebands into the same frequency, improving the signal-to-noise ratio (see Appendix B for details). The squared signal is then passed through a low-pass filter to allow for proper downsampling. Finally, the samples are stored in the memory of the relay for analysis in the data processing phase.

While the relay is gathering data, it also monitors the frequency of the power system and the alpha current magnitude to ensure that the motor operates under steady-state conditions.

D. Data Processing Phase

Fig. 9 shows the data processing logic. In the following discussion, the block numbers refer to the numbers circled in Fig. 9.

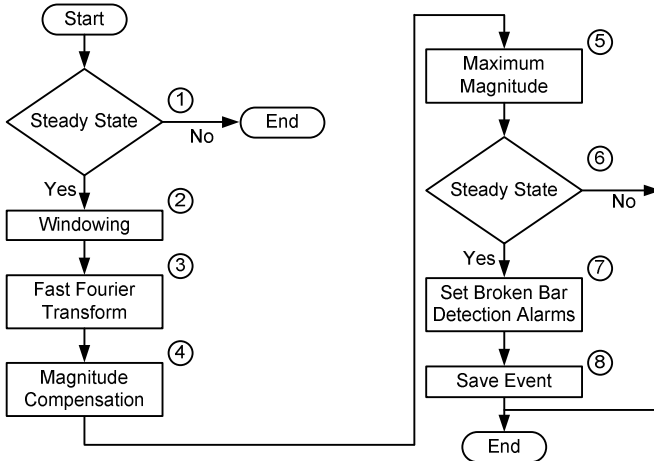


Fig. 9. Data processing phase.

1) Steady-State Verification (Block 1)

If the motor was not operating under steady-state conditions while the data were gathered, the data are not processed further.

2) Data Windowing (Block 2)

In this block, every value in the current buffer is multiplied by the corresponding element in a Hamming window of the same length. The elements of the Hamming window are computed using:

$$w(n) = 0.54 - 0.46 \cos\left(\frac{2\pi n}{N-1}\right) \quad (2)$$

where:

n is the location in the window.

N is the number of elements in the data window.

Fig. 10 shows the Hamming window and its effect on the data. Fig. 11 shows the effect of the Hamming window on the Fourier transform of the data. Note that the spectrum of the windowed signal is closer to the ideal spectrum than the spectrum of the original signal without windowing is.

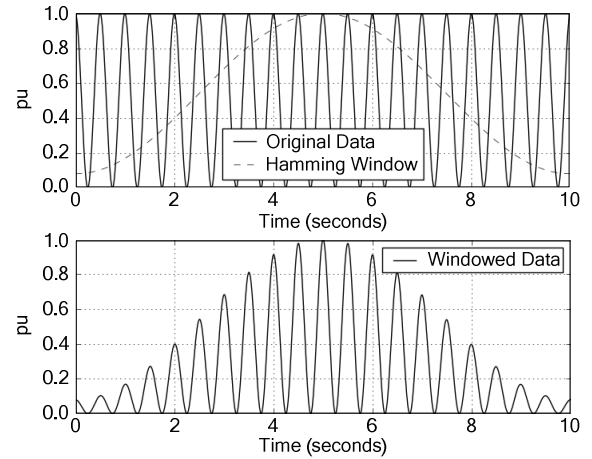


Fig. 10. Effect of data windowing in the time domain.

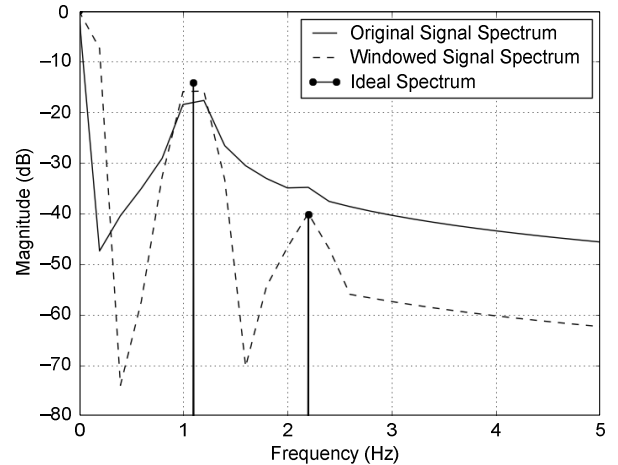


Fig. 11. Effect of data windowing in the frequency domain.

3) Fast Fourier Transform (Block 3)

This block computes the fast Fourier transform (FFT) of the samples on the I_α windowed data and then calculates the

magnitude associated with each frequency component. Fig. 12 shows the details of the data processing within the block.

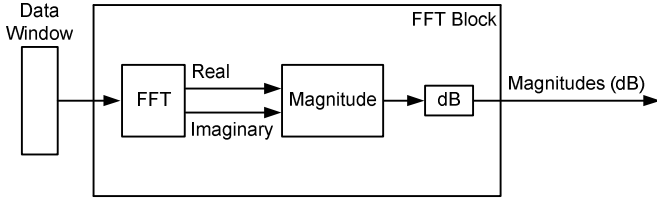


Fig. 12. Data flow in the FFT block.

4) Magnitude Compensation (Block 4)

This block compensates for the attenuation introduced by the low-pass filter in the data collection phase. The algorithm compensates the magnitudes of the frequency components between 0 and 7 Hz. The compensation factor for each frequency is obtained according to the low-pass filter attenuation at that frequency.

5) Maximum Magnitude Determination (Block 5)

This block takes two arrays as inputs. One of the arrays contains the frequencies to be studied. The second array contains the corresponding magnitudes. The algorithm first finds every local maximum and then returns the greatest maximum along with the associated frequency. If we let the array of magnitudes be $M = m[1], m[2], \dots, m[k]$, then every $m[i]$ that satisfies (3) is a local maximum.

$$m[i-1] < m[i] \text{ and } m[i] > m[i+1] \quad (3)$$

Equation (3) states that a point in the interval is a local maximum if it is greater than both the point to its left and the point to its right. Finally, the global maximum is the greatest of the local maximums. Fig. 13 shows a hypothetical frequency spectrum and identifies all the local maximums and the global maximum between 0 and 5 Hz.

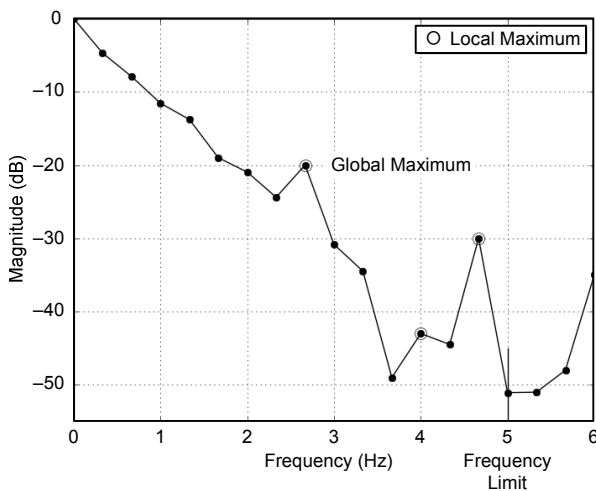


Fig. 13. Local and global maximums.

6) FFT-Based Steady-State Verification (Block 6)

In this block, the algorithm first computes the average magnitude (MAG_AVG) of the frequency components. Then it verifies that the average magnitude is below the healthy motor threshold. The algorithm also checks that the difference between the maximum and the average magnitudes is greater than the threshold MAR_AVGth. This second check helps to distinguish between noisy signals and signals that contain a small number of frequency components, such as broken bar conditions. Fig. 14 shows the thresholds on the frequency spectrum of a motor running at 50 percent load with one broken bar.

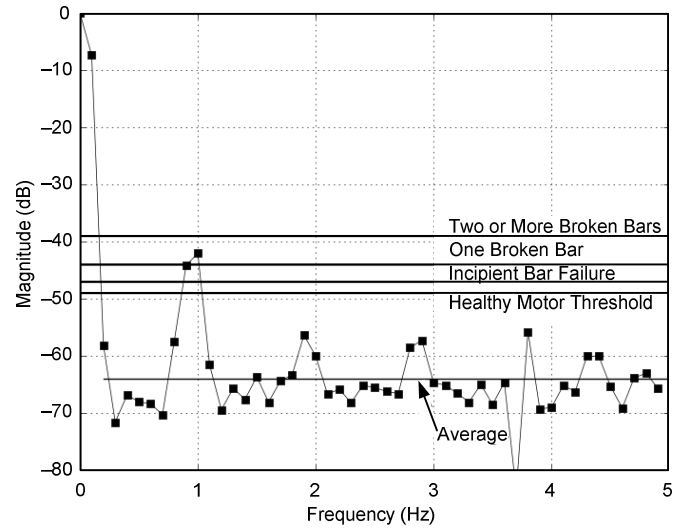


Fig. 14. Average magnitude and thresholds on the frequency spectrum of a motor running at 50 percent load with one broken bar.

Fig. 15 shows the logic diagram of the FFT-based steady-state detection function.

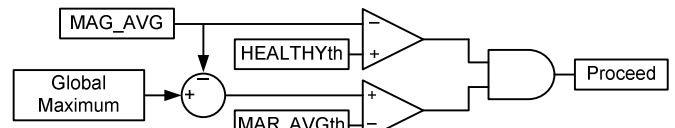


Fig. 15. FFT-based steady-state detection function.

In the logic in Fig. 15, HEALTHYth and MAR_AVGth are constants independent of the parameters of the protected motor.

We obtained the thresholds shown in Fig. 14 by taking into account data from [3], [11], and [12]; simulation results from a 5.5 kW and a 300 kW motor; and measurements from multiple industrial sites, including motors up to 1.656 MW.

The threshold names give a clear indication of the status of industrial squirrel cage induction motors. For other types of induction motors, the thresholds may not apply directly, but they still give an indication of the status of the rotor. For example, on a wound rotor induction machine, we can obtain broken bar current signatures by adding series resistances to

one phase of the rotor windings [13]. As the resistance introduced in the circuit grows, the magnitudes of the sidebands grow—possibly beyond the relay thresholds.

Fig. 16 shows the frequency spectrum of the currents of a 300 kW motor simulation (see Table I in Appendix A for the motor parameters). The magnitudes of the broken bar components of these simulations are lower than expected by the thresholds, but as the fault evolves from one to two and three bars, the algorithm clearly detects the fault.

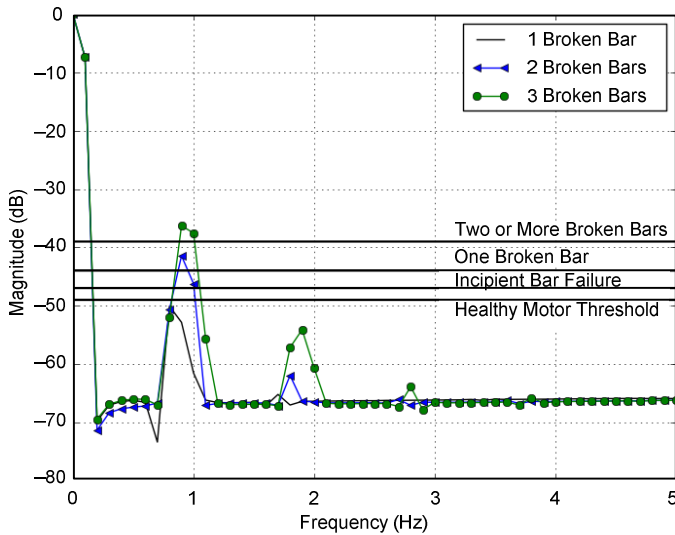


Fig. 16. Simulation of a 300 kW motor.

We show data from rotor bar failures at two industrial motors (see Table II in Appendix A for the motor parameters).

Fig. 17 shows the frequency spectrum of the currents of a 55 kW motor with four broken bars. Note that the magnitude of the broken bar frequency component is well above the Two or More Broken Bars threshold.

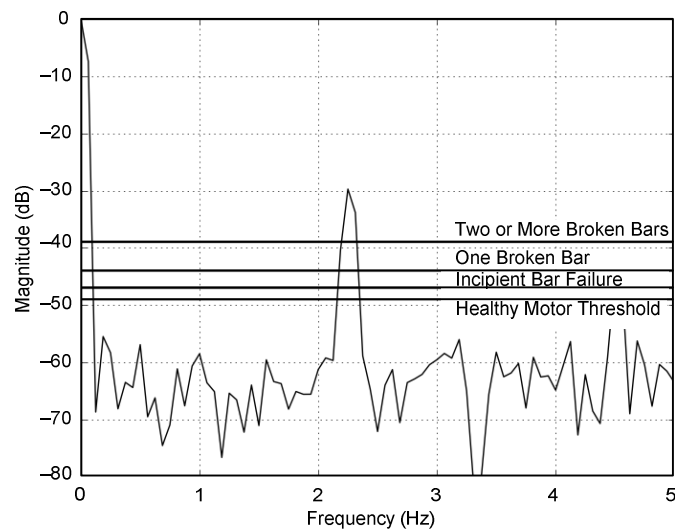


Fig. 17. 55 kW motor with four broken bars.

Fig. 18 shows the frequency spectrum of a 1.656 MW motor. These measurements were obtained long before the motor was taken out of service, so there is no broken bar count. However, we include these data to show that the algorithm will also detect problems in larger machines. When the 1.656 MW motor was taken out of service, five broken bars were found.

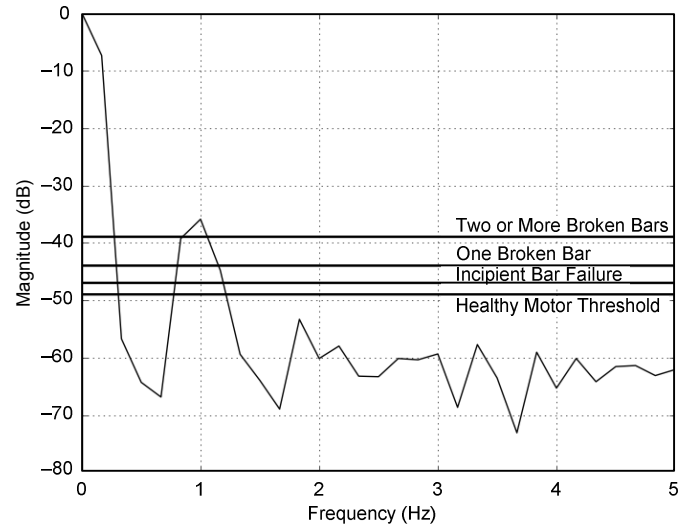


Fig. 18. Broken bar frequency components on a 1.656 MW motor.

7) Set Broken Bar Alarm Bits (Block 7)

In this block, the relay compares the maximum magnitude to the thresholds corresponding to incipient bar failure, one broken bar, and two or more broken bars. Finally, the relay updates the associated relay bits according to their respective thresholds.

8) Save Event (Block 8)

If any of the broken bar alarm bits assert, the relay records the maximum magnitude and associated frequency. Because these records are short (see Fig. 19), the relay can store several weeks of data.

Date	Time	Frequency (Hz)	Magnitude (dB)
8/10/2011	3:32PM	2.0	-33.2
8/10/2011	3:22PM	2.0	-33.2
.	.	.	.
6/10/2011	8:55AM	1.95	-39.6
6/10/2011	8:45AM	1.95	-39.3
.	.	.	.
4/10/2011	4:43PM	2.1	-45.7
4/10/2011	4:32PM	2.1	-45.6

Fig. 19. History of events.

IV. FOURIER TRANSFORM FUNCTION

The Fourier transform function is designed to provide protection engineers with detailed data about the behavior of

the motor. This function can be used to periodically collect motor status reports. Differences among historic reports can point to developing problems in the motor or the load. Comparing reports taken from a number of motors performing the same task can help to identify motor, load, and voltage supply problems.

Fig. 20 shows a block diagram for the Fourier transform function. First, the user selects a data source (any of the phase voltages or currents can be analyzed). Once the data source is selected, the relay collects data, as shown in Fig. 21. Then the data are multiplied by a Hamming window of the same length, and the Fourier transform is computed. The relay compensates the magnitudes for the attenuation of the low-pass filter and corrects the frequency according to the actual sampling rate that is a multiple of the system frequency.

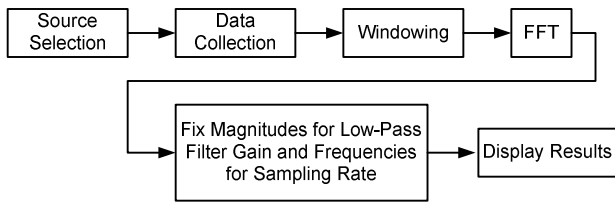


Fig. 20. Fourier transform function.

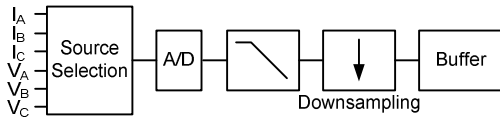


Fig. 21. Data collection for the Fourier transform function.

Finally, the relay displays the frequencies and their associated magnitudes and phase angles on its console port. The Fourier report includes the frequency components from 0 to 120 Hz. Fig. 22 shows the Fourier function output.

Selected Channel: IA		
Sample number	Amps	
1	86.97	
2	47.07	
3	-2.39	
.		
.		
.		
Frequency (Hz)	Magnitude (dB)	Angle (deg)
0.00	0.00	0.0
0.20	-73.23	0.0
0.40	-81.04	0.1
0.60	-80.61	0.1

Fig. 22. Fourier transform report.

V. DEPENDABILITY FOR MOTORS WITH LIGHT LOADS

The BBDE needs to distinguish between the 0 Hz component and the broken bar component at twice the slip frequency. When the motor is lightly loaded, the slip frequency is smaller than at full load and leads to a smaller

difference between the 0 Hz component and the broken bar component. The BBDE will not be able to distinguish the broken bar components when:

$$2s < D \quad (4)$$

where:

s is the operating slip frequency of the motor.

D is the minimum frequency difference at which we can distinguish between two frequency components.

If two frequency components are separated by less than D Hz, the associated frequency spectrum shows a single frequency component. The coefficient D is determined by the data window length and the windowing function used. In the BBDE implementation, D is 0.3 Hz and the algorithm does not distinguish the broken bar components when the motor load results in slip frequencies smaller than 0.15 Hz. Fig. 23 shows the minimum motor loading for which the BBDE will detect broken bars in three different motors.

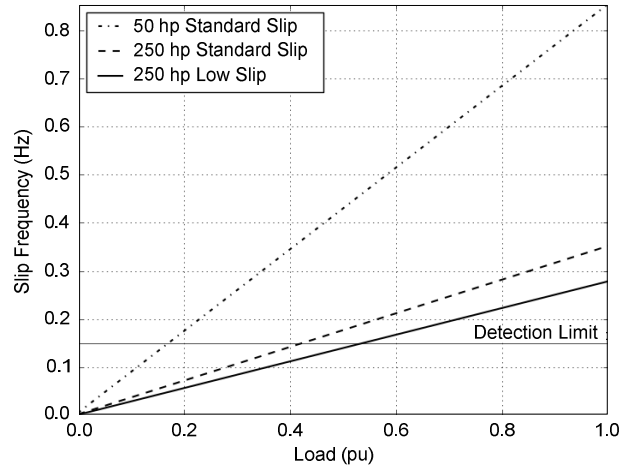


Fig. 23. The slip falls below the detection limit for motors with light load.

VI. EXPERIMENTAL RESULTS WITH ACTUAL MOTOR BROKEN BARS

A. Test Setup

To test the BBDE, we used the setup shown in Fig. 24. Fig. 25 shows the connection diagram of the setup. The motor protected by the BBDE is coupled to another motor driven by a commercial torque-controlled variable-speed drive that acts as a variable load.

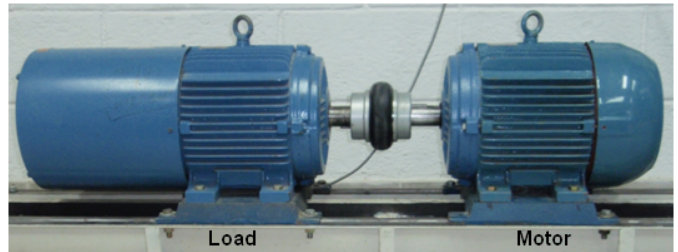


Fig. 24. Motor and its load for broken bar testing.

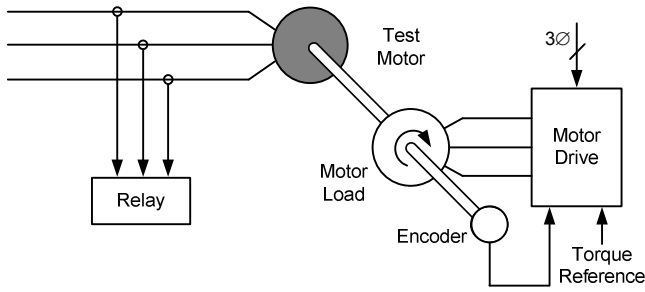


Fig. 25. Diagram of the test setup.

Fig. 26 shows the rotors used to test the BBDE. Note the holes drilled to break the bars. From left to right, Fig. 26 shows a healthy rotor and rotors with one, two, and three broken bars.

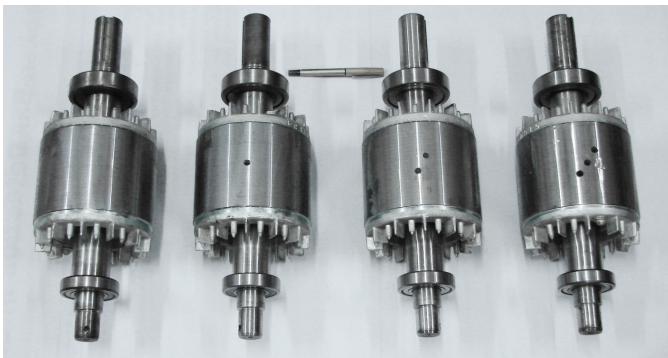


Fig. 26. Healthy rotor and rotors with one, two, and three broken bars.

B. Broken Bar Test Cases

These test cases show the typical broken bar behavior. As more bars break, the magnitudes of the sidebands grow, and as the load on the motor grows, the sideband components separate from the system frequency.

Fig. 27 compares the current frequency spectrum of a healthy motor with those of motors with one, two, and three broken bars. All of the current frequency spectrums correspond to motors running at 50 percent of the rated load. Note that the peak magnitudes grow as the number of broken bars increases, as expected.

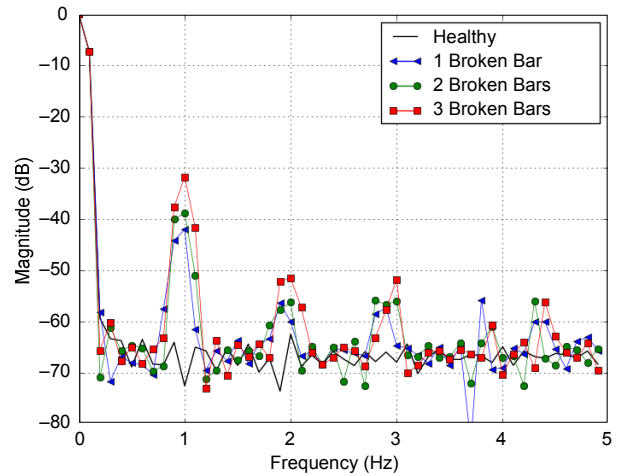


Fig. 27. The magnitudes of the sideband components grow with the number of broken bars.

Fig. 28 shows the frequency spectrum of the current of a motor with two broken bars at different loading levels. When this motor is fully loaded, the peak magnitude is located at around 2 Hz. As the loading level falls to 75 percent, 50 percent, and 25 percent, the frequency corresponding to the peak magnitude moves from 2 to 1.5 Hz, 1 Hz, and 0.5 Hz. When the motor is unloaded, the peak magnitude is not recognizable from the dc component of the spectrum at 0 Hz.

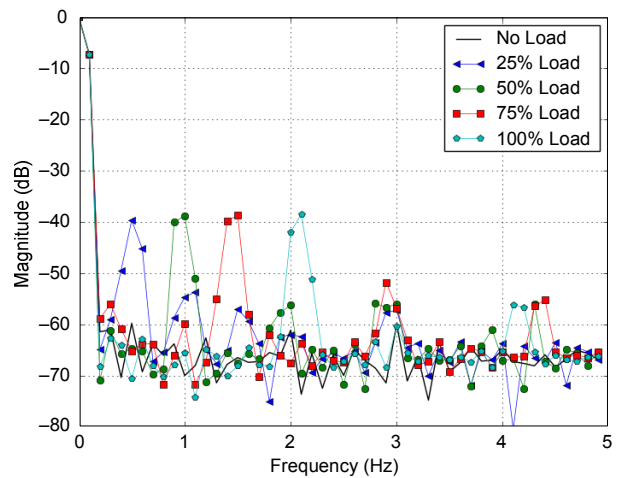


Fig. 28. The magnitude of the largest frequency component does not change with the motor load, but the frequency at which the maximum magnitude occurs does.

To show that the model accurately represents broken bar faults, we ran these same five cases in the model. Fig. 29 shows the frequency spectrum associated with the simulations. While the noise in the simulations is below -90 dB, the frequencies and magnitudes of the broken bar components closely match those presented in Fig. 28.

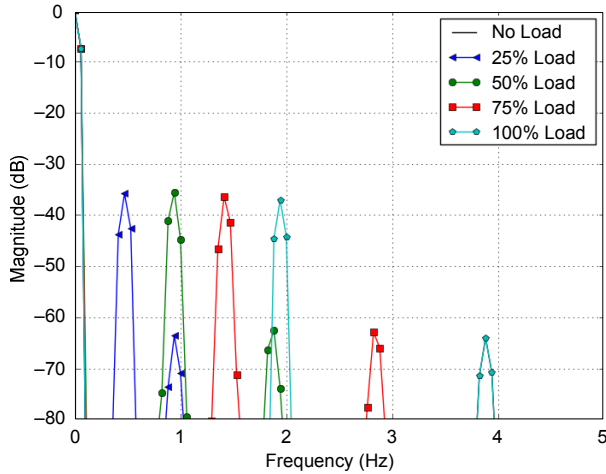


Fig. 29. Frequency spectrums corresponding to the simulation of a motor with two broken bars and different loading levels.

C. Security During Motor Starts

Fig. 30 shows the frequency spectrum of the starting current of a healthy motor. For comparison, it also shows the spectrum of a healthy motor under steady-state conditions.

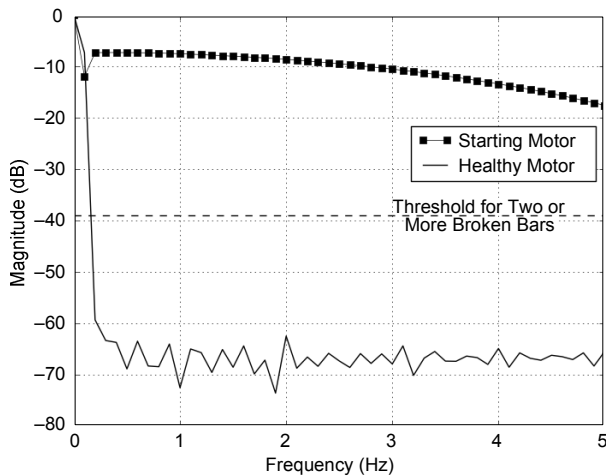


Fig. 30. Frequency spectrum during motor start and steady-state conditions.

Note that the magnitudes of the frequency components of the motor starting currents are greater than the thresholds for motors with broken bars. However, this case causes no false alarms because this condition is reliably detected by the current magnitude verification and by the FFT-based steady-state detection logic shown in Fig. 15.

D. Low-Frequency Voltage Oscillations

Low-frequency voltage oscillations cause currents similar to those caused by broken bars. To test the BBDE when the supply voltage contains these oscillations, we included a second motor and drive set, as shown in Fig. 31. The two motors are fed by the same autotransformer. By using the oscillatory torque reference on Drive 2, we can cause mechanical load oscillations on motor M_2 . The load oscillations cause current oscillations through the autotransformer, which lead to voltage oscillations at M_1 , the motor protected by the BBDE.

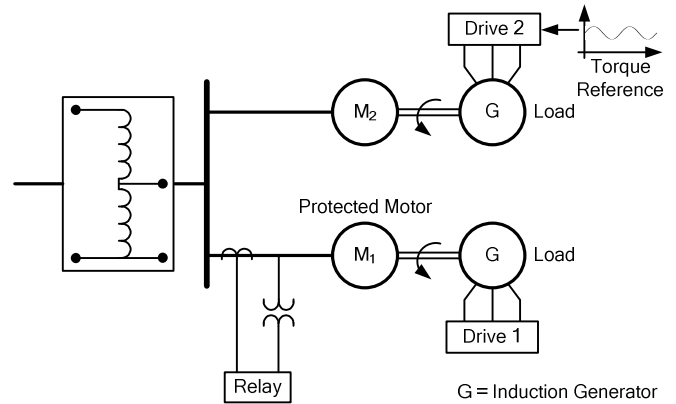


Fig. 31. Test setup to generate low-frequency voltage oscillations.

Fig. 32 shows the frequency spectrum of the current of a motor operating with a voltage source with a 1.5 percent magnitude, 2 Hz ripple. For comparison, it also shows the spectrum of the currents of a motor running at 100 percent load with three broken bars and a clean voltage source. Because the two spectrums are very similar, the BBDE does not distinguish between one case and the other, yet there are several strategies to differentiate the two, including the following:

- If all the motors connected to the same feeder show the same current spectrum, then the problem is likely an oscillation in the supply voltage.
- Voltage measurements farther away from the motor and closer to the source will confirm the presence of low-frequency components on the supply voltage.
- These low-frequency voltage oscillations may not be present in the system all the time. They typically appear when the system is heavily loaded or very lightly loaded. If the BBDE picks up only during those times, it is likely to pick up because of voltage oscillations.

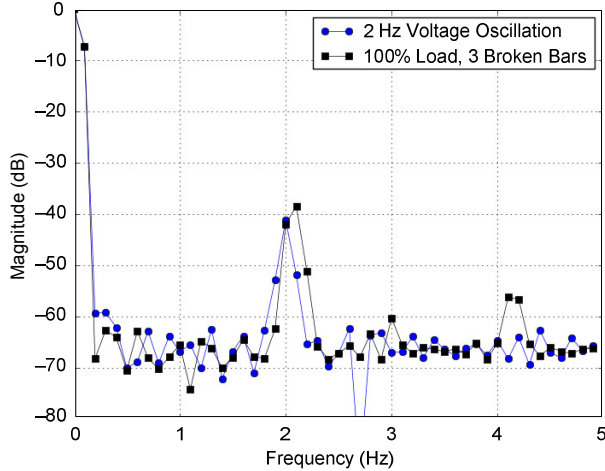


Fig. 32. Load frequency voltage oscillations can appear as a broken bar condition.

E. Low-Frequency Load Oscillations

Fig. 33 shows the frequency spectrum associated with a motor running a load that oscillates at 1 Hz. Note that the current signature is similar to that of a motor with three broken bars operating at 50 percent capacity. Load oscillations produced by an abnormal mechanical load condition (unbalance and misalignment), load characteristics (e.g., reciprocating loads), or a defective transmission generate a speed oscillation at the perturbation frequency (f_i), which is also seen as sideband components at $\pm f_i$ in the current spectrum [11] [14]. Thus, if the frequency of the speed oscillation is close to twice the slip frequency, as shown in Fig. 33, the BBDE will pick up for a nonbroken bar condition.

In some cases, broken bar conditions can be separated from load oscillations through the analysis of sidebands at higher current harmonics [12] [15]. If two or more motors are performing the same task, the spectrums of the motors can be compared to quantify the effect of the load on the spectrum. Then a greater-than-normal frequency component may indicate a broken bar condition.

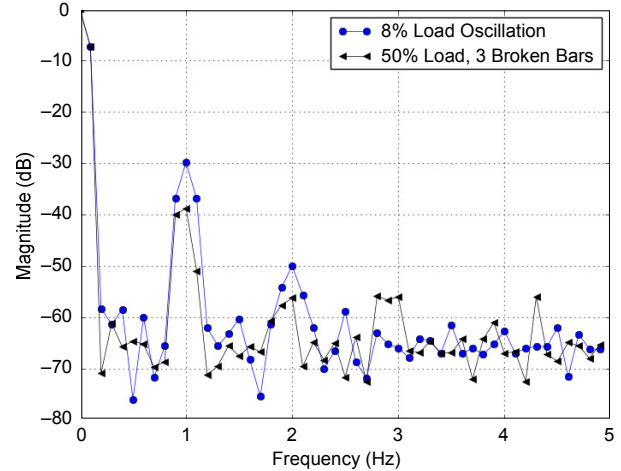


Fig. 33. Load oscillations can appear as a broken bar condition.

VII. CONCLUSION

The broken bar detection element with zero settings, along with the event history and the Fourier transform function, allows us to detect broken rotor bars under a wide variety of motor conditions. The detection element identifies the most common broken bar cases. The event history shows when problems start and how they evolve. Specific cases, such as when the voltage contains low-frequency components or when the motor drives an oscillating load, still require expert analysis. For these cases, the Fourier transform function speeds up the measurement process because no extra measurement equipment needs to be connected to the motor.

VIII. APPENDIX A

Table I shows the nameplate data and parameters of the 5.5 kW three-phase motor used in the laboratory tests and computer simulations, along with the nameplate data and parameters of the 300 kW motor used in computer simulations.

TABLE I
MOTOR PARAMETERS

Parameter	5.5 kW Motor	300 kW Motor
Rated power	5.5 kW	300 kW
Rated voltage	380 V	380/660 V
Frequency	50 Hz	50 Hz
Rated current	11.1 A	529/305 A
Rated speed	1470 rpm	2970 rpm
Power factor	0.85	0.90
Rotor inertia	0.02 kgm ²	0.9178 kgm ²
Number of poles	4	2
Number of rotor bars	40	40
Number of stator slots	48	48
Stator winding	18 turns per coil, 2 coils per group, 4 groups per phase, step 1:10:12	4:3:3:3:6 turns per coil, 6 coils per group, 2 groups per phase, step 1:14:16:18:20:22:24, shunt connection
Skew	1 stator slot period	1 stator slot period
Air gap	0.45 mm	1.8 mm
Air gap average radius	75 mm	139.1 mm
Stator length	110 mm	390 mm
Stator resistance	1.12 Ω	12.6 mΩ
Stator leakage inductance	0.0028 H	1 μH
Rotor bar resistance	32 μΩ	33 μΩ
Rotor bar leakage inductance	0.28 μH	0.87 μH
End ring segment resistance	1.56 μΩ	0.54 μΩ
End ring segment leakage inductance	0.03 μH	0.03 μH

Table II shows the nameplate data and number of rotor bars of the motors from Fig. 17 and Fig. 18.

TABLE II
PARAMETERS OF FIELD MOTORS

Parameter	55 kW Motor	1.656 MW Motor
Power	55 kW	1656 kW
Voltage	380 V	2300 V
Frequency	50 Hz	50 Hz
Rated current	100 A	475 A
Rated speed	1475 rpm	1488 rpm
Power factor	0.88	0.91
Number of rotor bars	46	76

IX. APPENDIX B

This appendix shows how squaring the input signal improves the signal-to-noise ratio of the broken bar frequency component. To this end, we first show the effect of squaring a clean broken bar current signal. The clean broken bar current signal consists of a main component at the power system frequency and two sidebands of smaller magnitude at each side of the main frequency component. We then introduce noise to the signal by adding a single frequency component and showing that squaring the new signal attenuates the noise component with respect to the broken bar component.

We begin by considering a clean broken bar current signal, given by:

$$s(t) = M \cos(2\pi f_o t) + m \cos(2\pi(f_o + f_d)t) + m \cos(2\pi(f_o - f_d)t) \quad (5)$$

where:

- M is the magnitude of the main component.
- m is the magnitude of each of the sidebands.
- f_o is the operating frequency.
- f_d is the separation between the main frequency component and the two sidebands.

The Fourier transform of $s(t)$ is given by:

$$F(s(t)) = \frac{M}{2} [\delta(2\pi f - 2\pi f_o) + \delta(2\pi f + 2\pi f_o)] + \frac{m}{2} [\delta(2\pi f - 2\pi(f_o + f_d)) + \delta(2\pi f + 2\pi(f_o + f_d))] + \frac{m}{2} [\delta(2\pi f - 2\pi(f_o - f_d)) + \delta(2\pi f + 2\pi(f_o - f_d))] \quad (6)$$

where:

f is the independent variable.

δ is the delta Dirac function.

Fig. 34 shows $F(s(t))$. To find $F(s(t)^2)$, we use the convolution theorem, which states that:

$$F(s(t)^2) = F(s(t)) * F(s(t)) \quad (7)$$

The convolution theorem determines that the magnitude of the dc component of $F(s(t)^2)$ is $\frac{M^2}{2} + m^2$ and the magnitude of the frequency component at f_d is Mm . There are also smaller frequency components at $\pm 2f_d$. As shown in Fig. 34, the frequency component pattern around the dc component also appears around $\pm 2f_o$. In this study, we are not concerned about these higher-frequency components because they are filtered out by the low-pass filter shown in Fig. 8.

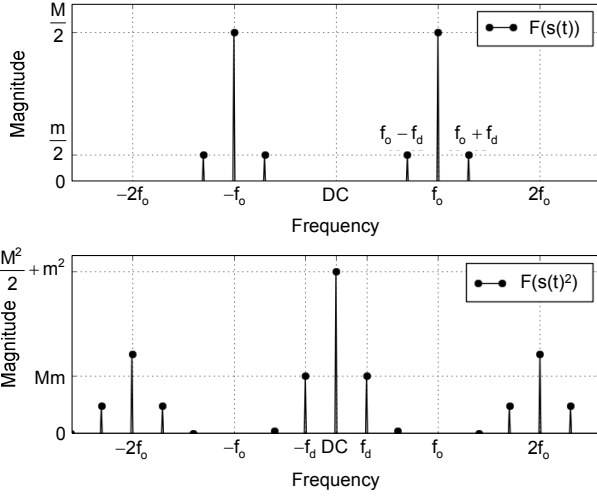


Fig. 34. Full spectrum of the Fourier transform of $s(t)$ and $s(t)^2$.

Now, we consider the signal:

$$\hat{s}(t) = s(t) + m \cos(2\pi(f_o + f_n)t) \quad (8)$$

where the added term represents a noise component of the same magnitude as the sidebands in $s(t)$. In this explanation, we use $f_n = \frac{f_d}{2}$ because it leads to the largest noise components in the convolved spectrum.

Convolving $\hat{s}(t)$, we obtain two new frequency components: one at f_n with magnitude $\frac{Mm + m^2}{2}$ and one at

$(f_d + f_n)$ with magnitude $\frac{m^2}{2}$. We study the component at f_n

because it is greater than the $(f_d + f_n)$ component. Then we define the signal-to-noise ratio as the magnitude of the broken bar component divided by the noise component. As shown in Fig. 35, for $\hat{s}(t)$, both magnitudes are the same and the ratio is 1. For $\hat{s}^2(t)$, on the other hand, the signal-to-noise ratio turns

out to be $\frac{Mm}{\left(\frac{Mm}{2} + \frac{m^2}{2}\right)}$. Fig. 35 shows that this ratio is greater

than 1, or more generally:

$$1 < \frac{Mm}{\frac{Mm}{2} + \frac{m^2}{2}} \quad (9)$$

$$\frac{Mm}{2} + \frac{m^2}{2} < Mm$$

$$\frac{1}{2}(Mm + m^2) < Mm$$

$$Mm + m^2 < 2Mm$$

$$m^2 < Mm$$

$$m < M$$

which means that the ratio will be larger than 1 as long as the magnitudes of the noise and the sidebands are less than the magnitude of the central component.

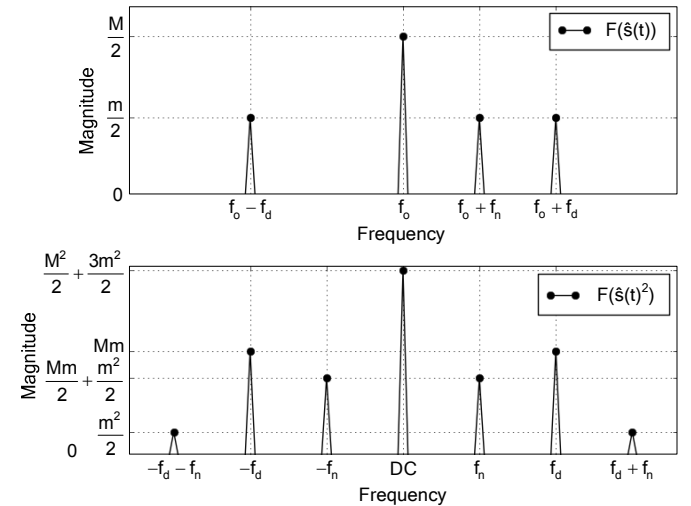


Fig. 35. Effect of squaring a signal with a noise component.

X. REFERENCES

- [1] R. M. McCoy, P. F. Albrecht, J. C. Appiarius, and E. L. Owen, "Improved Motors for Utility Applications, Volume I: Industry Assessment Study: Update and Analysis," Electric Power Research Institute, Palo Alto, CA, EL-4286, vol. 1 (RP-1763-2), September 1985.
- [2] O. V. Thorsen and M. Dalva, "A Survey of Faults on Induction Motors in Offshore Oil Industry, Petrochemical Industry, Gas Terminals, and Oil Refineries," *IEEE Transactions on Industry Applications*, vol. 31, no. 5, pp. 1186–1196, September/October 1995.
- [3] A. H. Bonnett and G. C. Soukup, "Analysis of Rotor Failures in Squirrel-Cage Induction Motors," *IEEE Transactions on Industry Applications*, vol. 24, no. 6, pp. 1124–1130, November/December 1988.
- [4] H. Penrose, *Electrical Motor Diagnostics*, 2nd ed. Success by Design, May 2008.
- [5] G. B. Kliman, R. A. Koegl, J. Stein, R. D. Endicott, and M. W. Madden, "Noninvasive Detection of Broken Rotor Bars in Operating Induction Motors," *IEEE Transactions on Energy Conversion*, vol. 3, no. 4, pp. 873–879, December 1988.
- [6] W. Deleroi, "Der Stabbruch im Käfigläufer eines Asynchronmotors, Teil 1: Beschreibung mittels Überlagerung eines Störfeldes," *Archiv Für Elektrotechnik*, vol. 67, pp. 91–99, 1984.
- [7] R. R. Schoen and T. G. Habetler, "Effects of Time-Varying Loads on Rotor Fault Detection in Induction Machines," *IEEE Transactions on Industry Applications*, vol. 31, no. 4, pp. 900–906, July/August 1995.
- [8] X. Luo, Y. Liao, H. Toliyat, A. El-Antably, and T. A. Lipo, "Multiple Coupled Circuit Modeling of Induction Machines," *IEEE Transactions on Industry Applications*, vol. 31, no. 2, pp. 311–318, March/April 1995.
- [9] H. A. Toliyat and T. A. Lipo, "Transient Analysis of Cage Induction Machines Under Stator, Rotor Bar, and End-Ring Faults," *IEEE Transactions on Energy Conversion*, vol. 10, no. 2, pp. 241–247, June 1995.
- [10] G. R. Bossio, C. H. De Angelo, G. O. Garcia, J. A. Solsona, and M. I. Valla, "Effects of Rotor Bar and End-Ring Faults Over the Signals of a Position Estimation Strategy for Induction Motors," *IEEE Transactions on Industry Applications*, vol. 41, no. 4, pp. 1005–1012, July/August 2005.
- [11] W. Long, T. G. Habetler, and R. G. Harley, "A Review of Separating Mechanical Load Effects From Rotor Faults Detection in Induction Motors," proceedings of the IEEE International Symposium on Diagnostics for Electric Machines, Power Electronics, and Drives, December 2007.
- [12] C. H. De Angelo, G. R. Bossio, J. M. Bossio, and G. O. Garcia, "Broken Bar Detection in Single-Phase Reciprocating Compressors," proceedings of the 34th Annual Conference of IEEE Industrial Electronics, Orlando, FL, 2008.
- [13] P. Tavner, L. Ran, J. Penman, and H. Sedding, *Condition Monitoring of Rotating Electrical Machines*. The Institution of Engineering and Technology, London, UK, 2008.
- [14] M. Blodt, D. Bonacci, J. Regnier, M. Chabert, and J. Faucher, "On-Line Monitoring of Mechanical Faults in Variable-Speed Induction Motor Drives Using the Wigner Distribution," *IEEE Transactions on Industrial Electronics*, vol. 55, no. 2, pp. 522–533, February 2008.
- [15] B. Akin, U. Orguner, H. A. Toliyat, and M. Rayner, "Low Order PWM Inverter Harmonics Contributions to the Inverter-Fed Induction Machine Fault Diagnosis," *IEEE Transactions on Industrial Electronics*, vol. 55, no. 2, pp. 610–619, February 2008.

XI. BIOGRAPHIES

Carlos Pezzani received his electrical engineering degree and Ph.D. in engineering sciences from Universidad Nacional de Río Cuarto, Argentina, in 2007 and 2013, respectively. In 2007, he joined the Grupo de Electrónica Aplicada, Universidad Nacional de Río Cuarto. His research interest is in fault diagnosis on electric machines.

Pablo Donolo received his electrical engineering degree and his masters degree in engineering sciences from Universidad Nacional de Río Cuarto, Argentina, in 2006 and 2013, respectively. In 2005, he joined the Grupo de Electrónica Aplicada, Universidad Nacional de Río Cuarto. He is also currently with Consejo Nacional de Investigaciones Científicas y Técnicas (CONICET). His research interest is in fault diagnosis on electric machines. Pablo is a student member of IEEE.

Guillermo Bossio received his electrical engineering degree from Universidad Nacional de Río Cuarto, Argentina, in 1999, and his doctorate of engineering degree from the Universidad Nacional de La Plata, Argentina, in 2004. Since 1994, he has been with the Grupo de Electrónica Aplicada, Facultad de Ingeniería, Universidad Nacional de Río Cuarto. He is also currently with Consejo Nacional de Investigaciones Científicas y Técnicas (CONICET), Argentina. His research interests include fault diagnosis on electric machines, ac motor drives, electric vehicles, and renewable energy generation. Guillermo is a member of IEEE.

Marcos Donolo received his BSEE from Universidad Nacional de Río Cuarto, Argentina, in 2000, and his masters degree in electrical engineering (2002), his masters degree in mathematics (2005), and his Ph.D. in electrical engineering (2006) from the Virginia Polytechnic Institute and State University. Since 2006, he has been with Schweitzer Engineering Laboratories, Inc. in Pullman, Washington, where he is presently a lead research engineer. He is a senior member of IEEE.

Armando Guzmán received his BSEE with honors from Guadalajara Autonomous University (UAG), Mexico. He received a diploma in fiber-optics engineering from Monterrey Institute of Technology and Advanced Studies (ITESM), Mexico, and his MSEE and MECE from the University of Idaho, USA. He served as regional supervisor of the Protection Department in the Western Transmission Region of the Federal Electricity Commission (the Mexican electrical utility company) in Guadalajara, Mexico, for 13 years. He lectured at UAG and the University of Idaho in power system protection and power system stability. Since 1993, he has been with Schweitzer Engineering Laboratories, Inc. in Pullman, Washington, where he is a research engineering manager. He holds numerous patents in power system protection and metering. He is a senior member of IEEE.

Stanley E. (Stan) Zocholl has a B.S. and an M.S. in Electrical Engineering from Drexel University. He is an IEEE Life Fellow and a member of the Power Engineering Society and the Industrial Application Society. He is also a member of the Power System Relay Committee and past chairman of the Relay Input Sources Subcommittee. He joined Schweitzer Engineering Laboratories, Inc. in 1991 in the position of Distinguished Engineer. He was with ABB Power T&D Company Allentown (formerly ITE, Gould BBC) since 1947, where he held various engineering positions, including Director of Protection Technology.

His biography appears in Who's Who in America. He holds over a dozen patents associated with power system protection using solid-state and microprocessor technology and is the author of numerous IEEE and protective relay conference papers. He received the Power System Relaying Committee's Distinguished Service Award in 1991. He was the Chairman of PSRCW G J2 that completed the AC Motor Protection Tutorial. He is the author of two books, *AC Motor Protection*, second edition, ISBN 0-9725026-1-0, and *Analyzing and Applying Current Transformers*, ISBN 0-9725026-2-9.